Supporting Information

Advancing Extreme-Temperature-Tolerant Zinc-Air Batteries through Photothermal Transition Metal Sulfide Heterostructures

Yuqing Zhong,[#] Yunzheng Zhang,[#] Jiajian Wang,[#] Huile Jin, Shuang Pan, Shun Wang,* Yihuang Chen**

College of Chemistry and Materials Engineering, Wenzhou University, Wenzhou 325035, China.

E-mail: yhchen@wzu.edu.cn; shunwang@wzu.edu.cn; shuangpan@wzu.edu.cn.

[#] Y.Zhong, Y.Zhang and J.Wang contributed equally to this work.

Experimental Section

1.1 Material selection

$CoSO_4 \cdot 7H_2O$ (> 99.5 %), ethylene glycol (EG), N,N-dimethylformamide (DMF; > 99.5 %), thiourea (> 99.0 %), $Ni(OAc)_2 \cdot 4H_2O$ (> 99.5 %), $Fe(NO_3)_3 \cdot 9H_2O$ (> 99.5 %), urea, $Ni(NO_3)_2 \cdot 6H_2O$ (> 99.5 %), GO, aqueous ammonia, KOH (> 95.0 %), zinc acetate dihydrate (> 99.5 %), and nafion solution (5 wt%) were purchased from Shanghai Mindrell Chemical Technology Co., Ltd.

1.2 Preparation of $NiCo_2S_4$@NiFeLDH/N-rGO

In the initial step, $NiCo_2S_4$ hollow spheres ($NiCo_2S_4$ HSs) were synthesized by dissolving 2 mmol of $CoSO_4 \cdot 7H_2O$ (0.562 g) in a 250 mL three-neck flask containing 80 mL of a mixed solvent with a V_{EG} (16 mL)/V_{DMF} (64 mL) volume ratio of 1:4. The mixture underwent a gradual heating process to reach 145 ℃within an argon atmosphere. Subsequently, a solution comprising 10 mmol of thiourea (0.7612 g) in 10 mL of mixed solvent was slowly added to the flask, maintaining reflux conditions for 5 hours. Following this, 10 mL of mixed solvent containing 1 mmol $Ni(OAc)_2$•4 H_2O (0.6167 g) was carefully dripped into the reaction solution, and the temperature sustained at 170 ℃ for an additional 5 hours. The resultant dark precipitate was collected through centrifugation, underwent multiple washes with deionized water and ethanol, and finally dried for 12 hours at 60 ℃ in a vacuum oven.

The $NiCo_2S_4$@NiFe LDH nanocomposites were synthesized through a single-step hydrothermal reaction process. Initially, a solution comprising 0.1346 g of $Fe(NO_3)_3 \cdot 9H_2O$, 0.2 g of urea, and 0.291 g of $Ni(NO_3)_2 \cdot 6H_2O$ dissolved in 34 mL of distilled water underwent magnetic stirring for 10 minutes. Subsequently, 0.219 g of $NiCo_2S_4$ hollow spheres were introduced into the solution and stirred continuously for an hour. The resulting solution was transferred into a 50 mL PTFE-lined stainless steel autoclave and maintained at 120 ℃ for 10 hours. Afterward, the solid product was washed with water and ethanol before being dried.

The preparation method for graphene oxide is based on an enhanced Hummer procedure. 2.5 g of graphite flakes and 1.2 g of sodium nitrate are introduced into a beaker with a capacity of 0.5 liters, which already contains 75 mL of concentrated sulfuric acid, and the mixture is maintained at a temperature of 0 ℃. Subsequently, mechanical stirring is employed before adding 8 g of KOH to the solution and continuing to stir for 5 hours. The temperature is then maintained at approximately 5 ℃ while the beaker is stirred for an additional hour at a temperature of 35 ℃, during which time a solution consisting of 160 mL ultra-pure water is gradually added dropwise. Following this step, the beaker undergoes stirring at a temperature of 98 ℃ for half an hour, after which it receives an addition of room-temperature ultra-pure water (200 mL) along with hydrogen peroxide (5 mL). Finally, the resulting feedstock undergoes centrifugation followed by cooling and dialysis until reaching neutral pH.

The synthesized $NiCo_2S_4$@NiFe LDH was then combined with N-rGO. To accomplish this, 16 mg of $NiCo_2S_4$@NiFe LDH, 8 mg of graphene oxide (dissolved in 1.8 mg/ml), 1 mL of ammonia, and 24 mL of ethanol were added to the stainless steel autoclave and allowed to react for 5 hours. The resulting suspension underwent three cycles of washing via ultrasonic centrifugation to yield the final product, $NiCo_2S_4$@NiFe LDH/N-rGO. The as-prepared $NiCo_2S_4$@NiFe LDH/N-rGO exhibited an obvious broad absorption band range from 350 nm to infrared region without obvious absorption peak or band edge in the UV-Vis-IR region (**Figure 2a**). This might be due to the fact that the material we prepared is black as a whole, resulting in a broad absorption band in the 350-800 nm region. Consequently, no obvious absorption peak or band edge can be observed.

1.3 Characterization

The morphology of $NiCo_2S_4$@NiFe LDH/N-rGO was analyzed using field emission transmission electron microscopy (TEM) and high-resolution transmission electron microscopy (HRTEM) performed on a JEOL 2100F instrument operating at 200 kV. The crystalline structure was characterized via X-ray diffraction (XRD) using a Bruker D8 advanced system. Brunauer-Emmett-Teller analysis was employed to

determine surface area and porosity distribution. Elemental composition and electronic states were investigated using X-ray photoelectron spectroscopy (XPS) measurements conducted on an SES 2002 instrument at 120 W power (8 mA, 15 kV). Raman spectra were acquired using a confocal Raman microscope (Horiba LabRAM HR Evolution) with an excitation wavelength of 532 nm and a power of 10 mW. For *operando* Raman spectroelectrochemistry, constant potentials were applied during electrolysis using a potentiostat (CHI 760E) within a Teflon electrochemical cell equipped with a quartz window. The setup comprised a working electrode (e.g., $NiCo_2S_4$@NiFe LDH/N-rGO) positioned at the top, a Pt wire counter electrode, and an Hg/HgO (1 M KOH) reference electrode. Spectral calibration was periodically performed using the silicon wafer (520.7 cm^{-1}) as a reference. Electrochemical measurements were carried out using an electrochemical station (CHI 760E).

1.4 Electrochemical Measurements

Cyclic voltammetry (CV)

All electrochemical assessments were performed in a three-electrode cell using a CHI760E electrochemical analyzer at room temperature. A rotary disk electrode (RDE) coated with catalysts, an Ag/AgCl (3 M KCl) or Hg/HgO (1 M KOH) electrode, and a graphite rod were utilized as the working electrode, reference electrode, and counter electrode, respectively. O_2-saturated 0.1 M KOH and O_2-saturated 1 M KOH were employed as the electrolytes for ORR and OER, respectively. For accurate measurements, iR correction was applied. The potentials of the Ag/AgCl or Hg/HgO electrodes were adjusted relative to the reversible hydrogen electrode (RHE). The conversion of the measured potential of the Ag/AgCl electrode to the potential versus the reversible hydrogen electrode (RHE) was calculated using the formula $E_{RHE} = E_{Ag/AgCl} + 0.21 + 0.0591$ pH-iR. Similarly, the measured potential of the Hg/HgO electrode was converted to the potential versus the reversible hydrogen electrode (RHE) using the formula $E_{RHE} = E_{Hg/HgO} + 0.098 + 0.0591$ pH-iR.

Rotating disk electrode (RDE) measurement

The glassy carbon electrode (GCE) was sequentially polished using alumina powders of different sizes: 1 μm, 0.3 μm, and 0.05 μm, prior to the electrochemical measurements. To create the catalyst slurry, 5.0 mg of the catalyst was dissolved in a solution consisting of 10 μL of Nafion solution and 990 μL of ethanol. Ultrasonication was carried out for 60 minutes to ensure proper mixing. Subsequently, this prepared slurry was deposited onto the GCE to fabricate the film electrode. The catalyst loading was maintained at 70 μg catalysts cm^{-2}. During electrochemical testing, the oxygen evolution reaction (OER) system was scanned from 0 V to 1.0 V (vs. Hg/HgO), while the oxygen reduction reaction (ORR) system was scanned from -1.0 V to 0 V (vs. Ag/AgCl). These measurements were conducted under varying rotating speeds: 400 rpm, 625 rpm, 900 rpm, 1225 rpm, 1600 rpm, and 2025 rpm, with a scanning rate of 5 mV s^{-1}.

The transferred electron number (n) in ORR was calculated from the slope of Koutecky-Levich (K-L) plot as follows.

(1) $J^{-1}=J_L^{-1}+J_K^{-1}=(B\omega^{1/2})^{-1}+J_K^{-1}$

(2) $B=0.2nFC_0(D_0)^{2/3}v^{-1/6}$

(3) $J_K=nFkC_0$

where J is the measured current density, J_K is the kinetic current density, ω is the rotation speed, n is the number of electron transfers, and F is Faraday Constant (F = 96485 C mol^{-1}), v is the kinetic viscosity (1.1×10^{-2} cm^2 s^{-1}), C_0 is the saturated concentration of oxygen in a 0.1 M KOH solution (1.2×10^{-3} mol L^{-1}), and D_0 is the diffusion coefficient of oxygen in a 0.1 M KOH solution (1.9×10^{-5} cm^2 s^{-1}). According to the above equation, the relation between J and ω can be obtained, and then the number of transferred electrons can be calculated. The EIS spectra of $NiCo_2S_4$@NiFe LDH/N-rGO were obtained at -0.2 V vs. Ag/AgCl and the frequency range varied from 0.01 to 100 kHz with 5 mV amplitude.

Rotating ring-disk electrode (RRDE) measurement

For the RRDE measurements, the disk electrode was scanned catholically at a rate of 5 mV s^{-1} and the ring potential was kept at 1.2 V vs. RHE. The percentage of

hydrogen peroxide *(%HO_2^-)* and the electron transfer number *(n)* were calculated according to the following equations:

$$(4)\ \%HO_2^- = \frac{200I_r}{NI_d I_r}$$

$$(5)\ n = \frac{4NI_d}{NI_d + I_r}$$

Where *Ir* is the ring current density, *Id* is the disk current density, and *N* is the collection efficiency for the Pt ring, which was determined to be 0.37. The experiments were conducted using rotating ring-disk electrode (DC-DSR ROTATOR, PHYCHEMI).

Photothermal experiment

To investigate the impact of photothermal assistance, the catalyst-loaded electrode were immersed in solution (e.g., 0.1 M or 1 M KOH) within a quartz reactor, and irradiated with an 808 nm near-infrared (NIR) light (MDL-H-808-5W). The temperature of the electrode was monitored using an IR thermal camera (FLIR E50) until reaching a stable temperature. When the electrode was immersed in the electrolyte, the temperature of the electrolyte near the polytetrafluoroethylene (PTFE) surface of the electrode increased slightly due to heat transfer between the electrode and the surrounding electrolyte, while the temperature of the rest of the electrolyte remained almost constant. The temperature of the rest of the electrolyte was recorded as the electrolyte temperature in Figure 2b. Except the experiments in Figure 2, the reactor was situated within a thermostatic water bath circulator, ensuring that the electrolyte remained at room temperature. The irradiation power could be adjusted within the range of 0 to 5.0 W cm^{-2}.

Photothermal conversion efficiency

To calculate the photothermal conversion efficiencies (PCEs), $NiCo_2S_4$@NiFe LDH/N-rGO was dispersed in water (Figure 2d-e). The PCEs of $NiCo_2S_4$@NiFe

LDH/N-rGO was calculated by the following equation:[1,2]

$$\eta = \frac{hA(T_{Max} - T_{Surr}) - Q_{Dis}}{I(1 - 10^{-A_{808}})}$$

where η is the photothermal conversion efficiency, h is the system heat transfer coefficient, A is the surface area of the container where heat exchange occurs, T_{Max} is the maximum temperature reached via laser illumination, T_{Surr} is the ambient temperature. Q_{Dis} is the energy transferred from system to environment, I is the laser power (2 W), A_{808} is the absorbance of $NiCo_2S_4$@NiFe LDH/N-rGO at 808 nm. hA is calculated by the following equation:

$$hA = \frac{\sum_i m_i C_{p,i}}{\tau_s}$$

m_i and $C_{p,i}$ are the mass and heat capacity of system components. In this work, water and cuvette are used as solvent and container, respectively (C_{water} = 4.2 J g^{-1} K^{-1}, $C_{cuvette} \approx$ 0.8 J g^{-1} K^{-1}).

τ_s is the system time constant which can be obtained by linearly fitting the plot of the time (t) against the negative natural logarithm of the driving force temperature (θ) during the cooling process after laser illumination. τ_s is the slope of the linearly fitting line and θ is calculated by the following equation:

$$\theta = \frac{T_{Surr} - T(t)}{T_{Surr} - T_{Max}}$$

Q_{Dis} is heat input due to light absorption by the solvent and container, which can be calculated by the following equation:[1,2]

$$Q_{Dis} = \frac{\sum_i m_i C_{p,i} \times (T_{\mathrm{Max},solvent} - T_{Surr})}{\tau_{s,solvent}}$$

where $\tau_{s,solvent}$ is obtained via the same way as τ_s but with solvent only (Figure 2f).

Zinc-Air Battery Test

The liquid ZAB was constructed utilizing zinc foil and carbon fiber paper loaded with $NiCo_2S_4$@NiFe LDH/N-rGO as the anode and cathode, respectively. During the

evaluation of the ZAB's performance, a rectangular section (0.5 cm × 0.8 cm) was excised from the zinc anode, leaving a rectangular aperture on the zinc foil. This allowed incident light directed towards the anode to penetrate through the rectangular hole on the zinc foil and reach the air cathode side. A 6 M KOH solution containing 0.2 M $Zn(Ac)_2$ served as the electrolyte, ensuring the reversible redox reaction of the Zn anode. The air electrode's catalyst loading was set at 1.0 mg cm^{-2}. Charge-discharge recyclability performance of liquid ZABs was assessed at different current densities with a 20-minute cycle duration. In photothermal-assisted electrochemical testing, the electrode loaded with catalyst materials was exposed to light for 3 min each time to ensure temperature equilibrium, followed by performance testing.

To assemble the flexible ZAB, the alkalinized hydrogel electrolyte based on polyacrylic acid (PAA) was first synthesized through a free-radical polymerization process as outlined below. Initially, 14.4 mL of acrylic acid (AA) was dissolved in 20 mL of water. Subsequently, a 10 mL solution of sodium hydroxide (20 M) was added dropwise while stirring at 0 °C. Then, 24 mg of N,N'-methylenebisacrylamide (MBAA), serving as a chemical cross-linker, and 220 mg of ammonium persulfate (APS), acting as the initiator, were introduced into the monomer solution. After stirring for 30 minutes at 0 °C, the mixture was degassed, sealed under argon (Ar), and polymerized at 65 °C for 2 hours. The resulting polymer was collected, dried, and subsequently immersed in a solution containing KOH (6 M) and $Zn(Ac)_2$ (0.2 M) for a specified duration. Utilizing the alkalinized PAA-based hydrogel as the electrolyte, zinc foil as the anode, and $NiCo_2S_4$@NiFe LDH/N-rGO loaded carbon cloth as the cathode, a quasi-solid-state flexible ZAB was fabricated. Following a procedure similar to that used for liquid ZAB, a 0.5 cm × 0.8 cm rectangular portion was cut out from the zinc anode during the flexible ZAB performance test, creating a rectangular hole. This enabled the NIR light from the anode side to pass through the opening and reach the air cathode side. Charge-discharge recyclability performance of flexible ZABs was assessed at different current densities with a 6-minute cycle duration.

All ZABs underwent investigation under ambient atmosphere conditions. Polarization curve measurements were conducted using linear sweep voltammetry

(LSV) at a scanning rate of 5 mV s^{-1} and a temperature of 25°C. The CHI760E electrochemical working station from CH Instruments was utilized for these measurements. Both the current density and power density were standardized concerning the effective surface area of the air electrode. Specific capacity calculations were performed using the following equations:

$$\frac{\text{current} * \text{service hours}}{\text{weight of consumed zinc}}$$

The energy density was calculated according the equation below:

$$\frac{\text{current} * \text{service hours} * \text{average discharge voltage}}{\text{weight of consumed zinc}}$$

Computational methods

The DFT calculation was performed using the Vienna ab-initio Simulation Package (VASP) with the Perdew-Burke-Ernzerhof (PBE) functional in the generalized gradient approximation (GGA) method to consider exchange dependent effects.[3-6] The projected augmented wave (PAW) method was used for kernel valence interaction, and a plane wave energy cutoff of 500 eV and a 3×3×1 k-point Monkhorst-Pack grid were employed for Brillouin zone sampling.[7] Additionally, a vacuum space of 15 Å was added to prevent periodic interactions on the surface. The structure will be optimized until reaching an energy convergence of 1.0×10^{-4} eV and a force convergence of 0.02 eV $Å^{-1}$.

The formula for calculating the change in Gibbs free energy (ΔG) at each step is as follows:

$$\Delta G = \Delta E + \Delta ZPE - T\Delta S$$

In the equation, ΔE represents the electronic energy difference directly calculated by DFT, while ΔZPE denotes the zero-point energy difference. The variable T corresponds to room temperature (298.15 K), and ΔS signifies the entropy change. The zero-point energy difference (*ZPE*) can be determined through frequency calculations.[8]

$$ZPE = \frac{1}{2}\sum hvi$$

Calculation of the *TS* value of adsorbent substances based on vibration frequency[9]:

$$TS = k_B T \left[\sum_k ln(\frac{1}{1 - e^{-h\nu/k_B T}}) + \sum_k \frac{h\nu}{k_B T} \frac{1}{(e^{h\nu/k_B T} - 1)} + 1 \right]$$

Figures and Tables

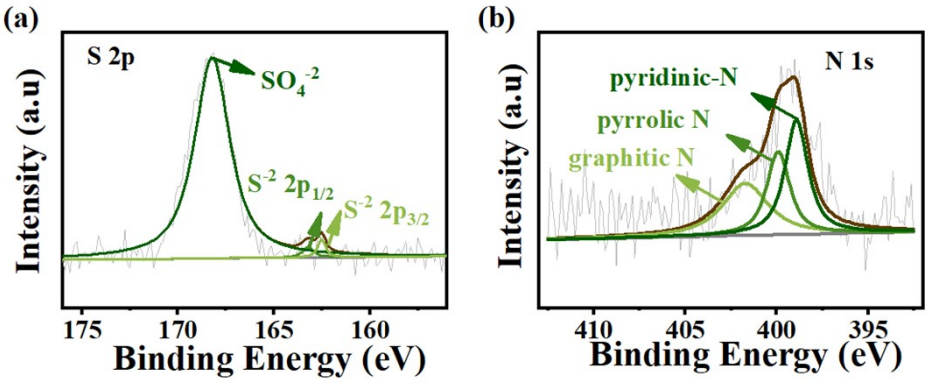

Figure S1. High-resolution XPS spectra of (a) S 2p spectrum, (b) N 1s spectrum in the $NiCo_2S_4$@NiFe LDH/N-rGO.

For the S 2p spectrum of $NiCo_2S_4$@NiFe LDH/N-rGO, the peaks at 163.0 and 161.6 eV are attributed to S^{2-}, and the peaks at 168.0 eV are from sulfate **(Figure S1a)**. The high-resolution N 1s spectrum can be further divided into three subpeaks centered on 397.78 eV (pyridinic N), 398.91 eV (pyrrolic N), and 399.79 eV (graphitic N). Studies have proved that pyridinic nitrogen and graphitic nitrogen have excellent electron-receiving ability, which can promote the adsorption of oxygen, thereby reducing the overpotential. Pyridinic and pyrrolic N with lone pairs of electrons can be used as metal coordination **(Figure S1b)**.

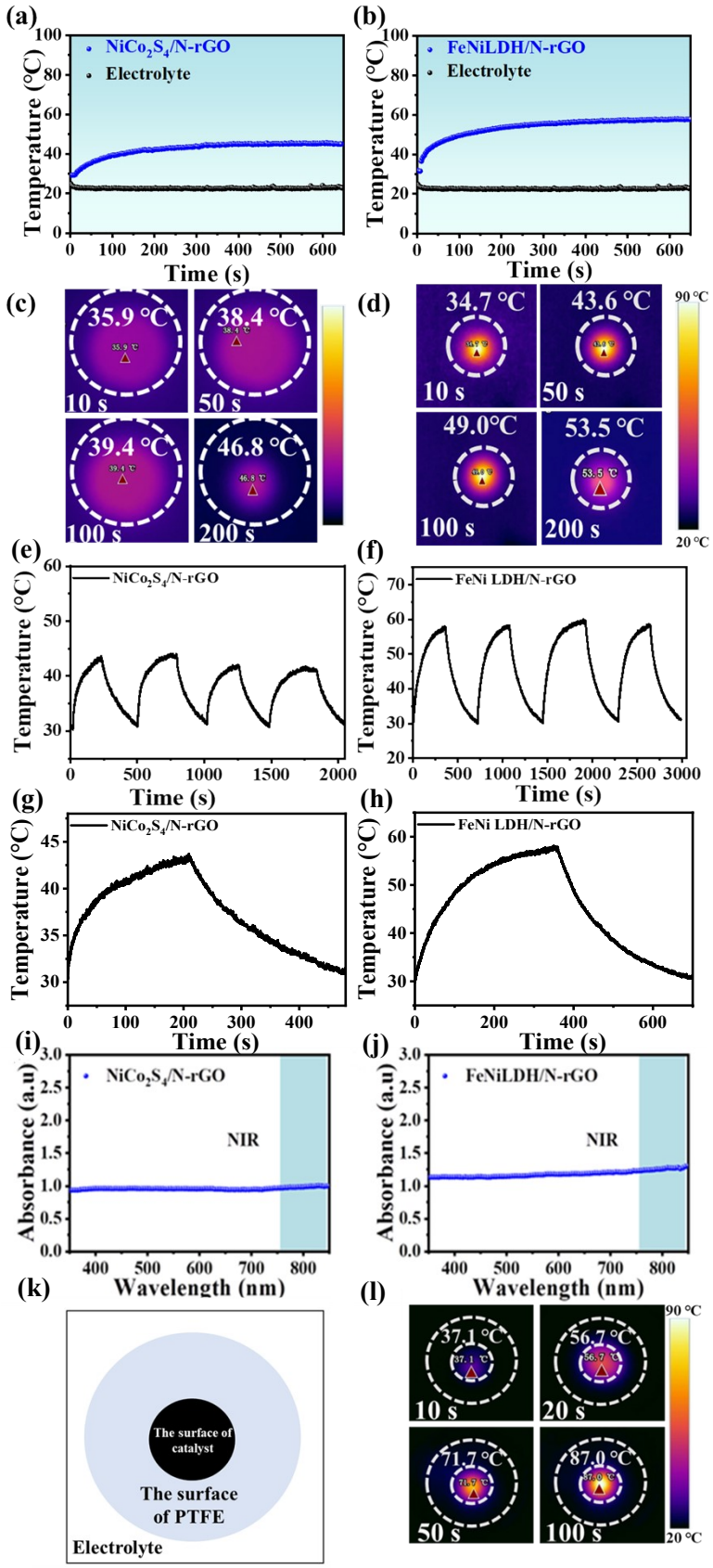

Figure S2. (a) Temperature change of electrode loaded with $NiCo_2S_4$-based photothermal material in electrolyte and electrolyte solution over time under 808 nm

NIR irradiation. (c) Corresponding infrared images of $NiCo_2S_4$-based electrode in electrolyte at different times. (e) Photothermal stability of $NiCo_2S_4$-based photothermal material dispersed in water during four times of heating and cooling under 808 nm laser irradiation. (g) The photothermal conversion curve of $NiCo_2S_4$/N-rGO in water. (i) UV-Vis absorption spectrum of $NiCo_2S_4$-based photothermal material in water. (b) Temperature change of electrode loaded with NiFe LDH-based photothermal material in electrolyte and electrolyte solution over time under 808 nm NIR irradiation. (d) Corresponding infrared images of NiFe LDH-based electrode in electrolyte at different times. (f) Photothermal stability of NiFe LDH-based photothermal material dispersed in water during four times of heating and cooling under 808 nm laser irradiation. (h) The photothermal conversion curve of NiFe LDH-based photothermal material in water. (j) UV-Vis absorption spectrum of NiFe LDH-based photothermal material in water. (k) The scheme of rotary disk electrode (RDE) with catalyst in electrolyte. (l) Corresponding infrared images of electrode in the electrolyte solution at different time. The areas of PTFE and $NiCo_2S_4$@NiFe LDH/N-rGO were indicated by dashed outer and inner circles, respectively.

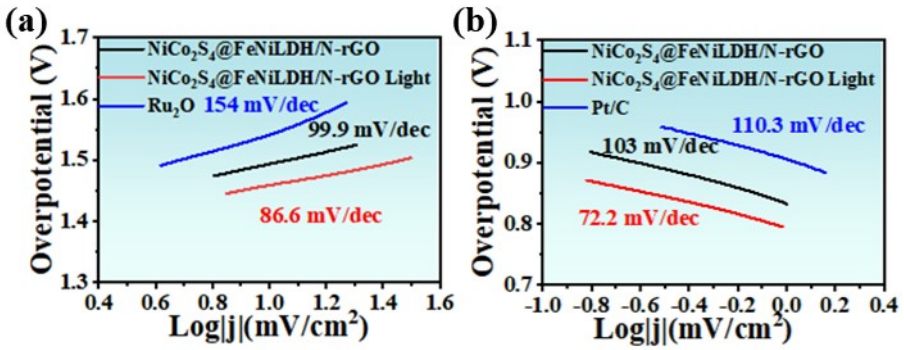

Figure S3. Tafel curves of varied electrodes for (a) OER in 1 M KOH and (b) ORR in 0.1 M KOH.

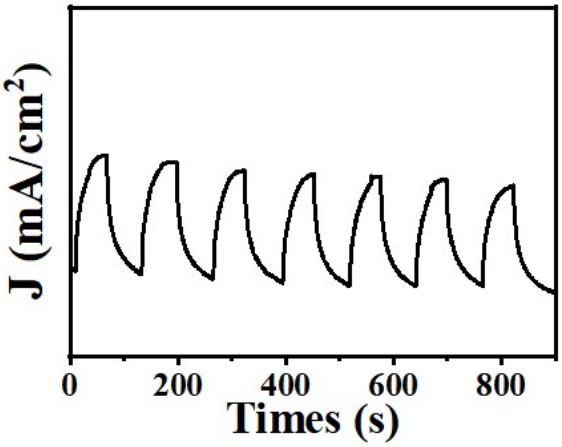

Figure S4. Current density over time of $NiCo_2S_4$@NiFe LDH/N-rGO electrode at a potential of 1.52 V_{RHE} under intermittent illumination.

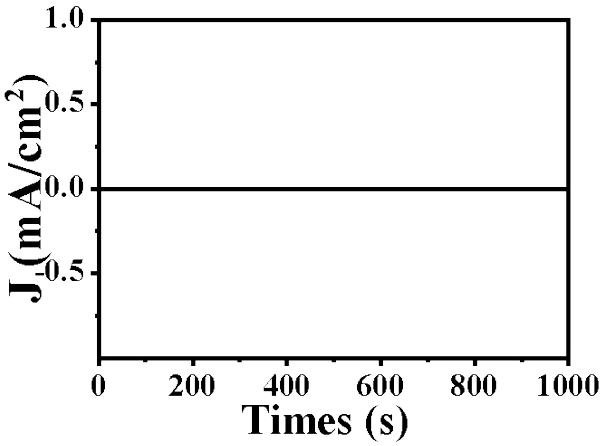

Figure S5. Photocurrent density for the $NiCo_2S_4$@NiFe LDH/N-rGO electrode under illumination at applied voltages below 1.23 V.

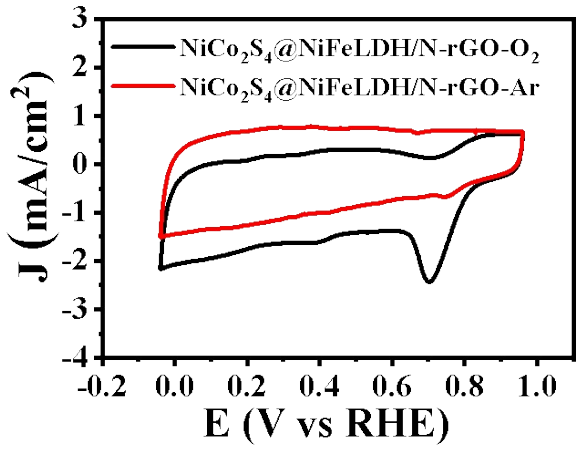

Figure S6. CV of $NiCo_2S_4$@NiFe LDH/N-rGO in O_2 or Ar saturated 0.1 M KOH solutions. An obvious oxygen reduction peak at 0.702 V vs RHE was observed in the O_2-saturated solution rather than Ar-saturated electrolyte, revealing the potential high ORR performance of $NiCo_2S_4$@NiFe LDH/N-rGO.

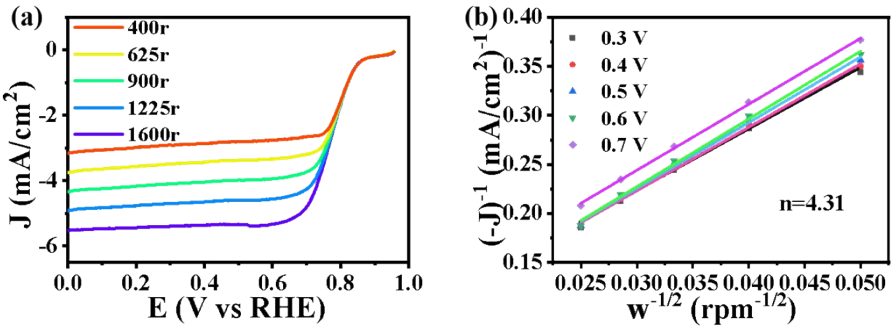

Figure S7. (a) ORR LSV curves at different rotational speeds of $NiCo_2S_4$@NiFe LDH/N-rGO. (b) The corresponding Koutecky-Levich plots at different potentials.

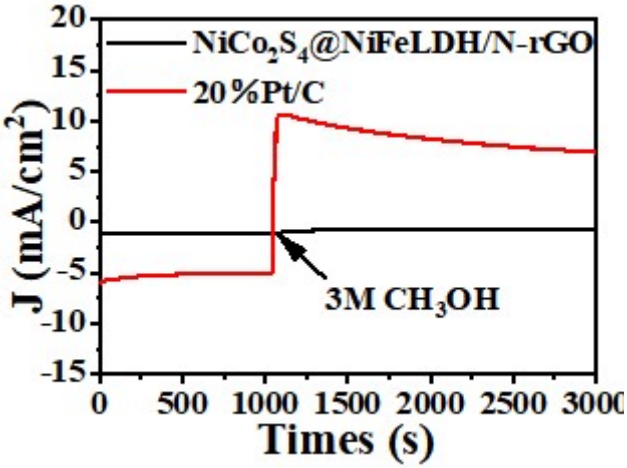

Figure S8. Methanol resistance test of $NiCo_2S_4$@NiFe LDH/N-rGO and Pt/C.

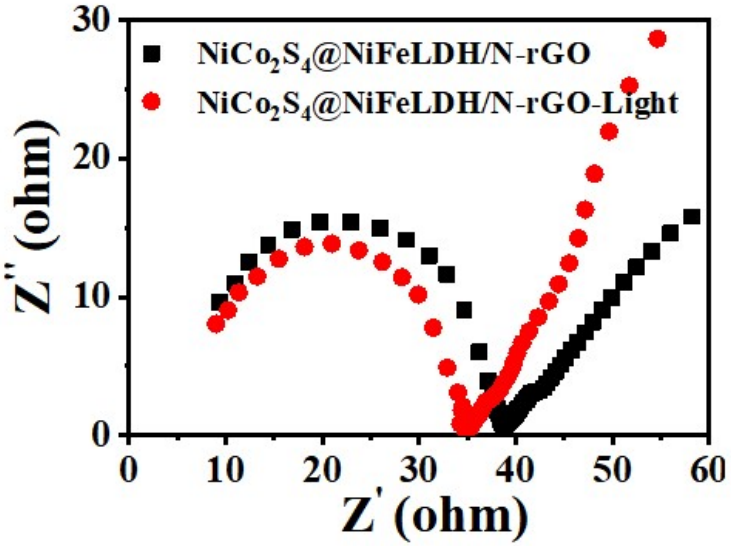

Figure S9. EIS for $NiCo_2S_4$@NiFe LDH/N-rGO with and without NIR laser irradiation.

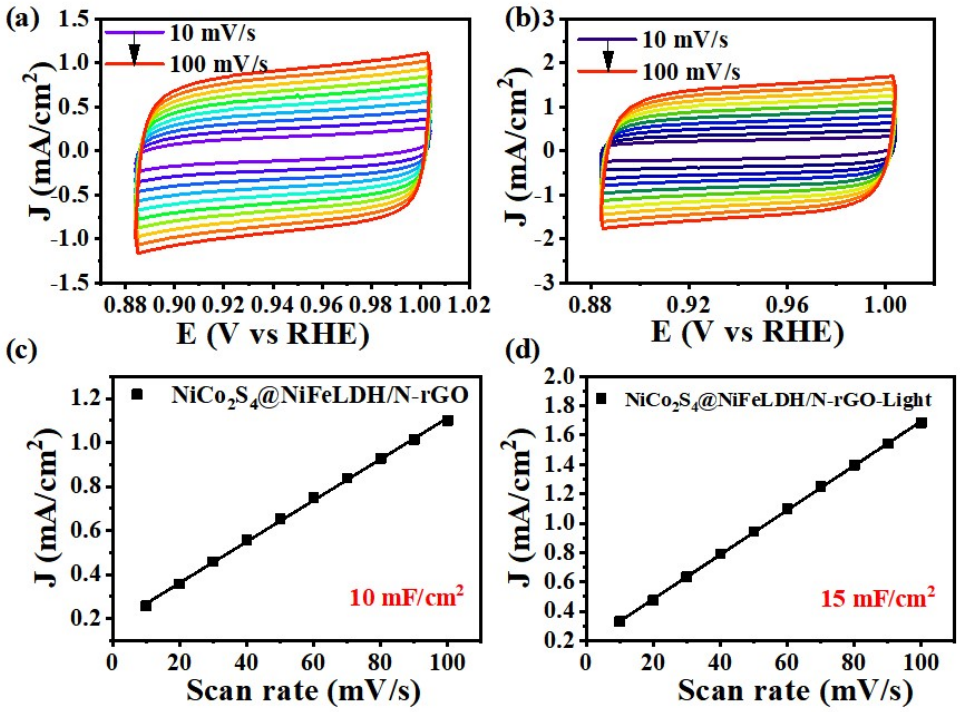

Figure S10. CV curves of electrodes with different scanning rate: (a) $NiCo_2S_4$@NiFe LDH/N-rGO without light, (b) $NiCo_2S_4$@NiFe LDH/N-rGO with light, (c,d) corresponding double-layer capacitance data derived from CV measurements at different scan rate.

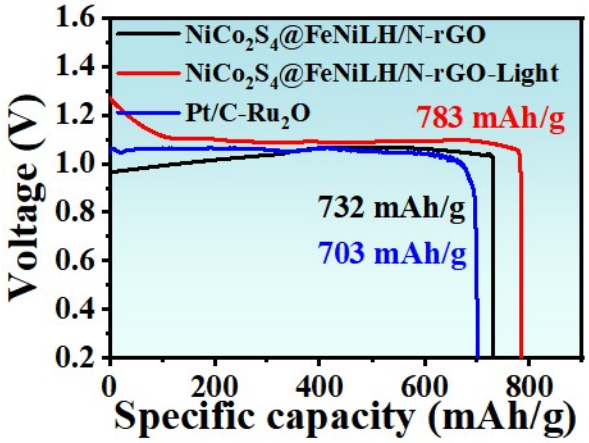

Figure S11. Specific capacities of ZABs at a current density of 10 mA cm^{-2} based on $NiCo_2S_4$@NiFe LDH/N-rGO with and without light, and Pt/C+RuO_2.

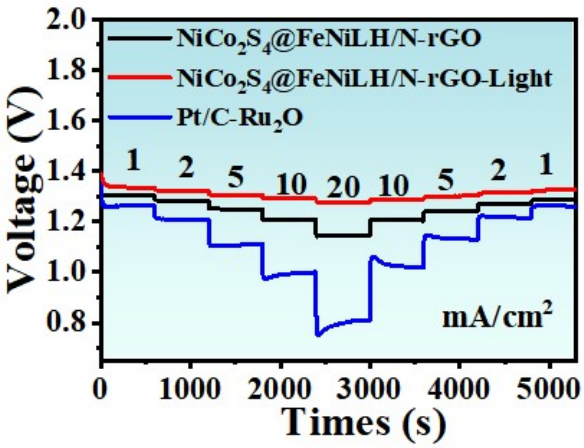

Figure S12. Discharging curves at different current densities of ZABs based on $NiCo_2S_4$@NiFe LDH/N-rGO with and without light, and Pt/C+RuO_2.

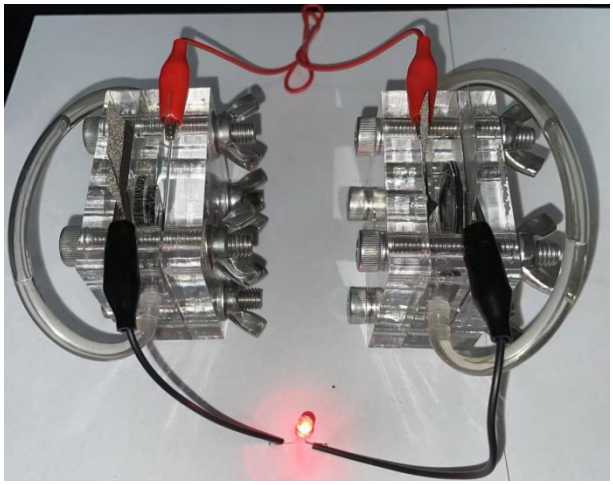

Figure S13. Digital image of a LED powered by two series-connected ZABs based on $NiCo_2S_4$@NiFe LDH/N-rGO.

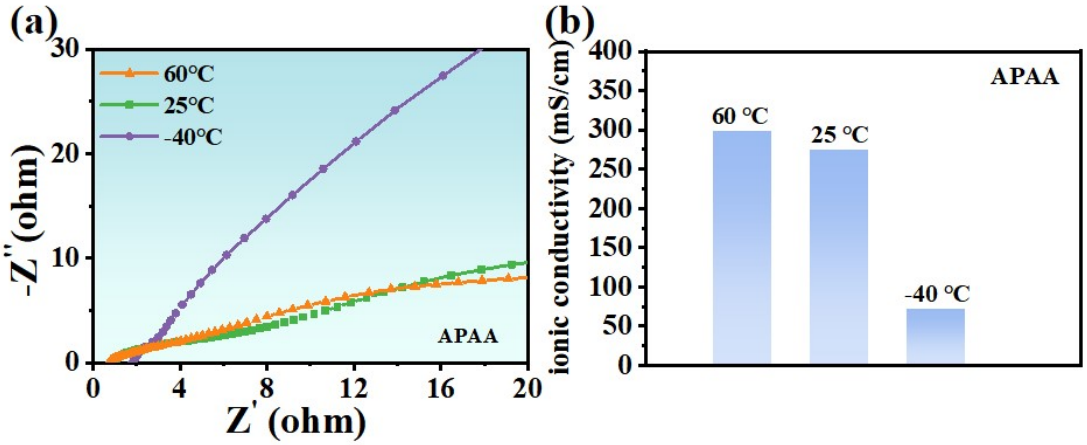

Figure S14. Conductivity of APAA hydrogels alkalized at 25 ℃, -40 ℃ and 60 ℃ in FZABs.

For the low-temperature application tests of flexible ZABs, an alkalized PAA-based hydrogel was used as the electrolyte. Considering the concentrated alkaline solute used in ZABs, the intrinsic colligative property of the solutions can be utilized to mitigate the problems caused by low-temperatures. Besides, the polarity of terminal groups in PAA was shown to be a critical factor for the anti-freezing property of the host hydrogel, steering the synthesis of a highly conductive and flexible hydrogel electrolyte with excellent cold-temperature adaptability. Thus the electrolytes do not freeze at low temperatures with large ionic conductivity at subzero temperatures (e.g., -40°C; **Figure S14**).

Similarly, the abundant hydrophilic functional groups within PAA-based hydrogels can form interaction forces (e.g., hydrogen bonds) with water molecules, which effectively trap the water within the hydrogel and slow down their evaporation rate at high temperatures, thereby exhibiting excellent water retention properties under such conditions. As the temperature increases, the hydrogel exhibited better ionic conductivity (**Figure S14**). As such, despite a certain degree of water evaporation, the test results demonstrated that the hydrogel electrolyte used in FZABs still operate normally at 60 ℃, thereby enabling long-term cycle performance.

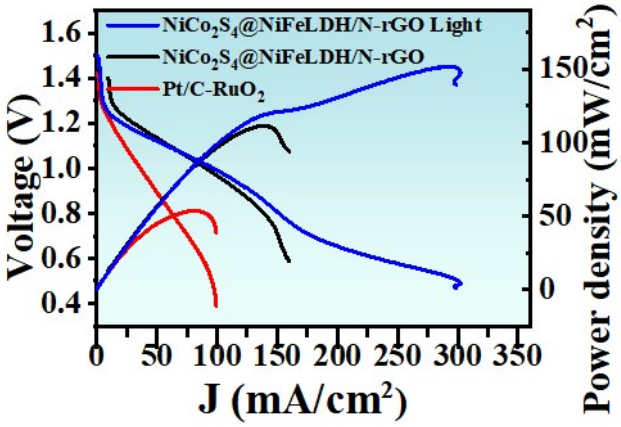

Figure S15. Discharge and power density diagram of FZABs at room temperature based on $NiCo_2S_4$@NiFe LDH/N-rGO with and without light, and Pt/C + RuO_2.

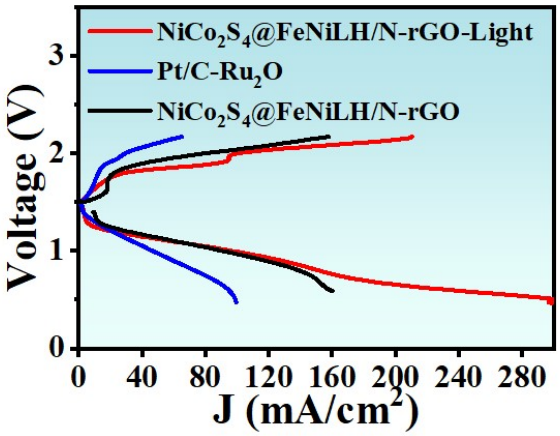

Figure S16. Charging/discharging polarization curves of FZABs at room temperature based on $NiCo_2S_4$@NiFe LDH/N-rGO and Pt/C + RuO_2.

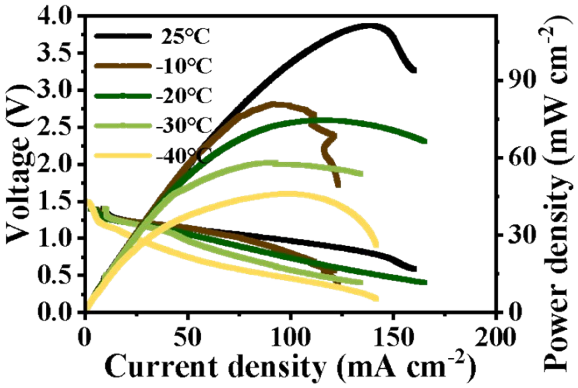

Figure S17. Discharge and power density diagrams of $NiCo_2S_4$@NiFe LDH/N-rGO-based FZABs at different temperatures.

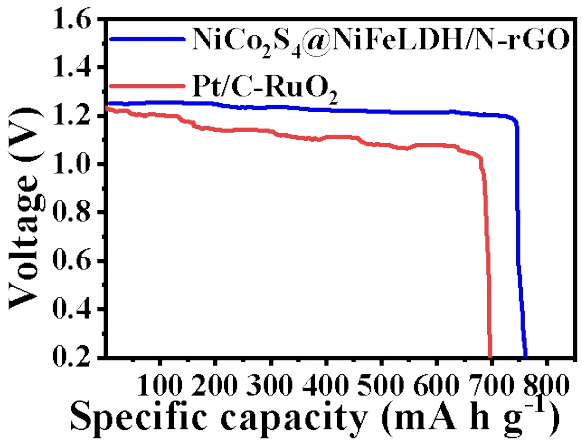

Figure S18. Specific capacities of FZABs at a current density of 1 mA cm^{-2} based on $NiCo_2S_4$@NiFe LDH/N-rGO and Pt/C + RuO_2.

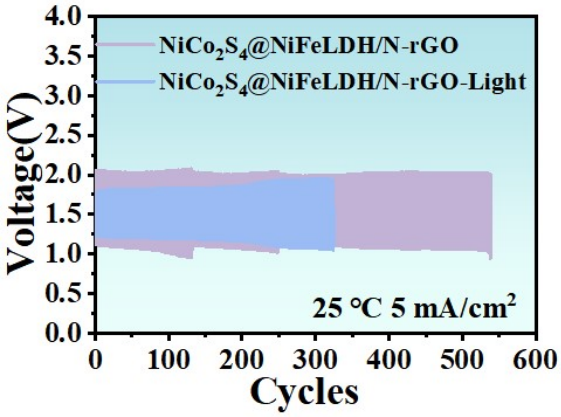

Figure S19. The cycling performance of $NiCo_2S_4$@NiFe LDH/N-rGO-based FZABs at 5 mA cm^{-2} with and without light at 25 ℃.

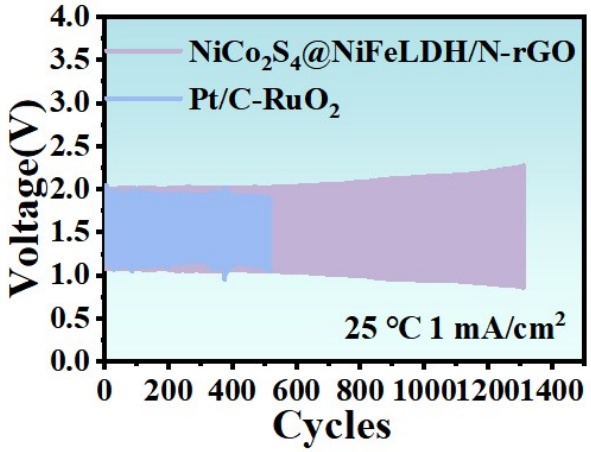

Figure S20. The cycling performance of FZABs based on $NiCo_2S_4$@NiFe LDH/N-rGO and Pt/C + RuO_2 at 1mA cm^{-2}.

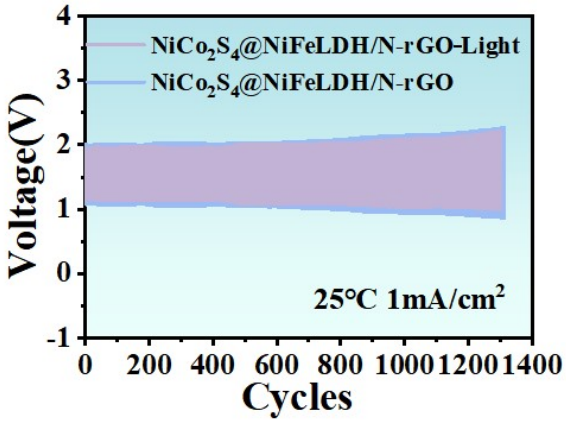

Figure S21. The cycling performance of $NiCo_2S_4$@NiFe LDH/N-rGO-based FZABs at 1 mA cm^{-2} with and without light at 25 ℃.

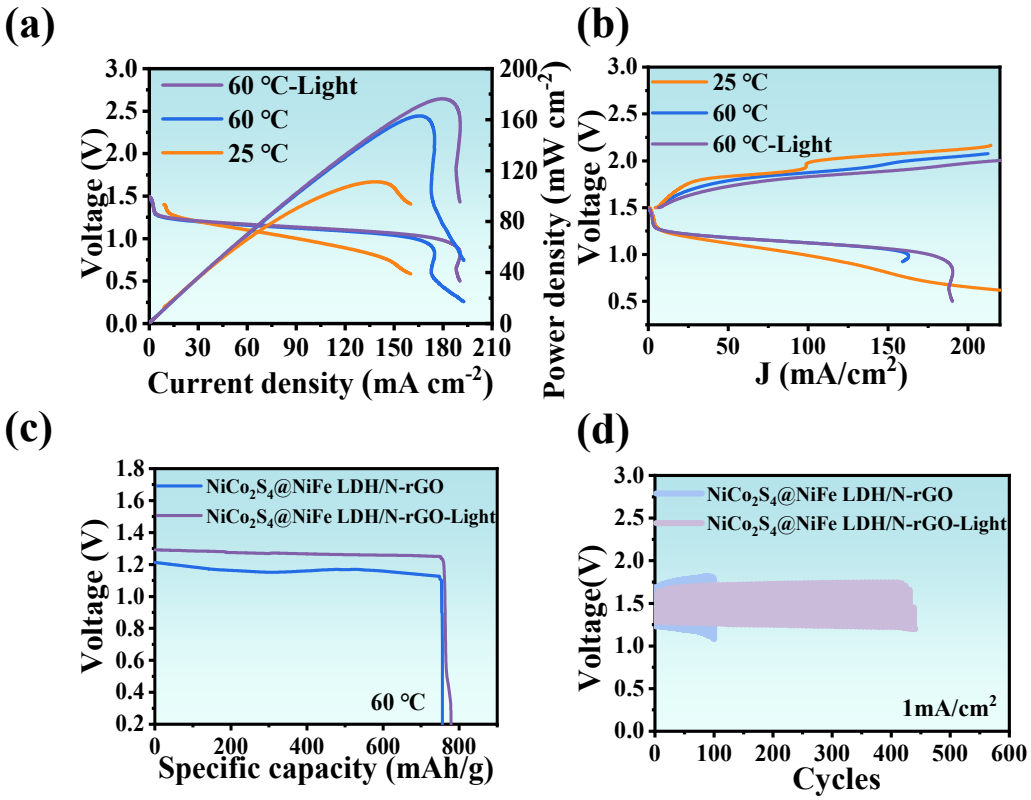

Figure S22. The performance of $NiCo_2S_4$@NiFe LDH/N-rGO-based FZABs at 25 and 60℃: (a) power density, (b) charge-discharge polarization curve, (c) specific capacity, and (d) cycling tests.

In order to investigate the applicability of solid-state batteries in high temperature environments, a FZAB composed of $NiCo_2S_4$@NiFe LDH/N-rGO was tested at 60 ℃ (**Figure S22**). Compared with a power density of 112 mW cm^{-2} at normal temperature (25 ℃), the power density increased to 162.9 mW cm^{-2} at high temperature (60 ℃) and further increased to 176.3 mW cm^{-2} with illumination (**Figure S22a**). By comparing the polarization curves for charge and discharge, it was observed that the polarization curve gap decreased at high temperature (60 ℃) than that of at room temperature (25 ℃), and further decreased under light exposure (**Figure S22b**). A specific capacity of 755.95 $mAhg^{-1}$ was obtained at a high temperature of 60 ℃, which further increased to 778.63 $mAhg^{-1}$ with illumination (**Figure S22c**). Stability testing of the FZABs at high temperature showed that the

efficiency reduced from an initial value of 72.8 % to 60.1 % after undergoing 100 cycles at a high temperature of 60 ℃. However, upon illumination, cycle stability improved significantly with an increase in round-trip efficiency from an initial value of 78.4 % to 69.8 % (**Figure S22d**).

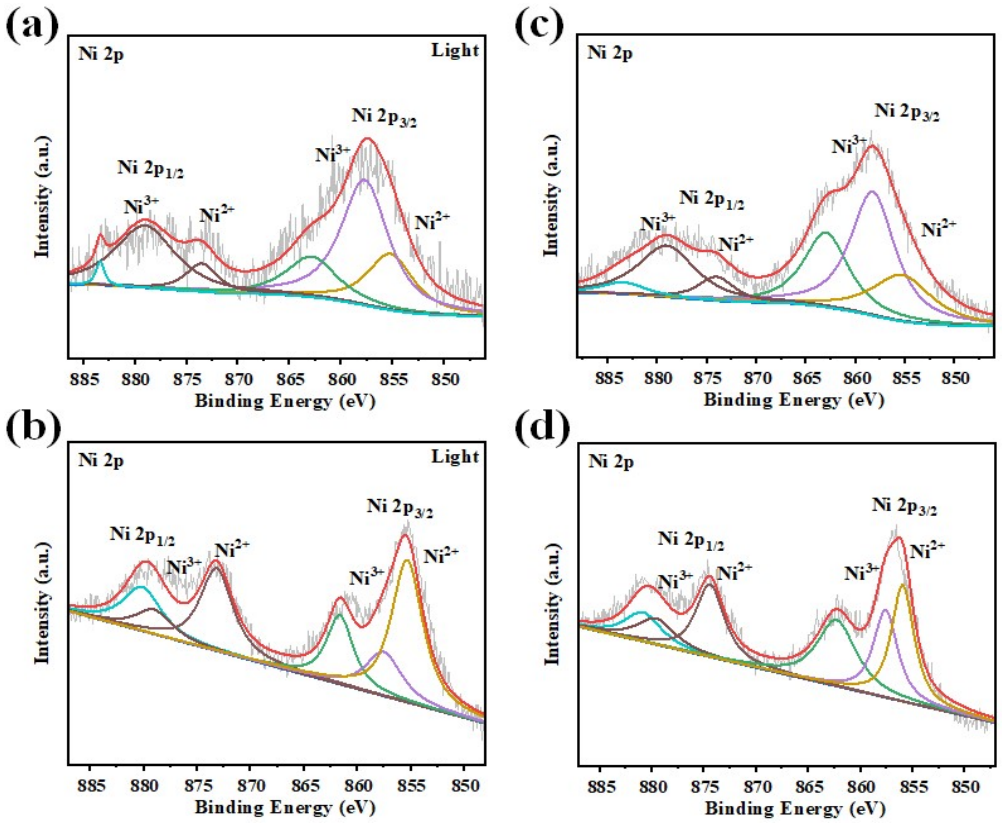

Figure S23. XPS spectra for Ni 2p of $NiCo_2S_4$@NiFe LDH/N-rGO after (a) photothermal-assisted OER and (b) subsequent photothermal-assisted ORR tests. XPS spectra for Ni 2p of $NiCo_2S_4$@NiFe LDH/N-rGO after (c) OER (without light) and (d) subsequent ORR tests (without light) as control experiments.

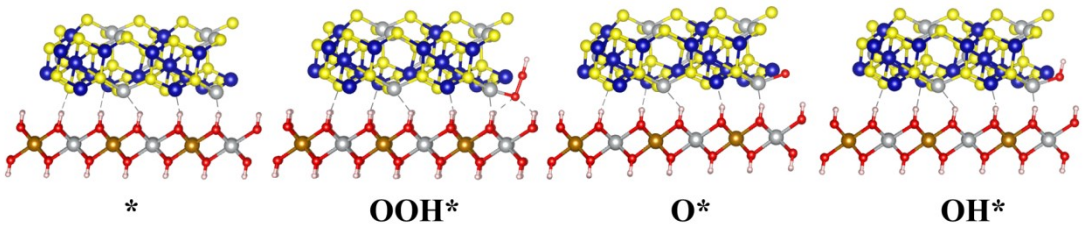

Figure S24. DFT optimized adsorption configurations of intermediates for $NiCo_2S_4$@NiFe LDH/N-rGO.

The shortest atom-to-atom distances of atoms in $NiCo_2S_4$ (i.e., Ni, Co, and S atoms) to their nearest atom in NiFe LDH were measured to be 2.02 Å, 1.84 Å, and 1.95 Å in **Figure S24**. Upon comparison, these atom-to-atom distances were consistent with the bond length of hydrogen-bonds and much smaller than the typical van der Waals (vdW) distance[10-11], suggesting the presence of interaction forces between between $NiCo_2S_4$ and NiFe LDH. Similarly, the shortest atom-to-atom distance for system in **Figure 6f** was measured to be 1.84 Å. As such, there were interaction forces between the two components in systems of **Figures 6f and S24**.

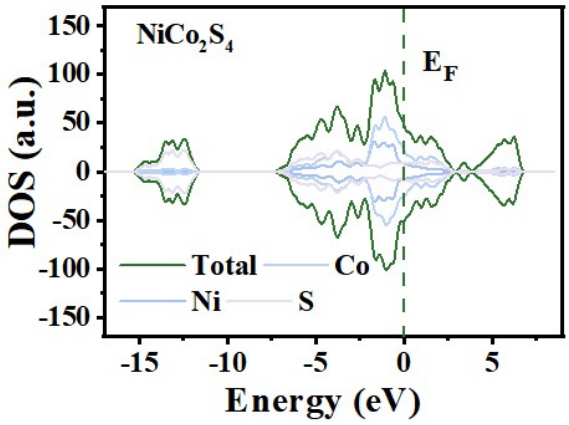

Figure S25. The DOS of $NiCo_2S_4$.

Table S1 Comparison of photothermal conversion efficiency of $NiCo_2S_4$@NiFe LDH/N-rGO with those advanced reported photothermal materials.

Materials	Wavelength (nm)	Photothermal conversion	Reference
$NiCo_2S_4$@NiFe LDH/N-rGO	808	82 %	*This work*
$NiCo_2S_4$/N-rGO	808	62.97 %	
NiFe LDH/N-rGO	808	76.58 %	
ICR-QuNPs	1000-1700	81.1%	*Advanced Materials.* ***2023****, 35, 2210179.*
AgNPs	808	78.6%	*Chemical Engineering Journal.* ***2024,*** *484, 149329*
$MoSe_2$ 2H/1T hybrid nanoparticles	808	38%	*Advanced Materials.* ***2023****, 35, 2301129.*
N-TiO_2	785	82%	*ACS Applied Energy Materials.* ***2024****, 7, 2918−2924*
Pd_8 Nanocluster	808	73.3%	*Angewandte Chemie International Edition.* ***2024****, 63, e202313491.*
QDI-NPs	808	64.7%	*Angewandte Chemie International Edition.* ***2019***, *58, 1638*
2TPE-2NDTA	808	54.9%	*Nature Communications.* ***2019****, 10, 768*
PPP-NDs	645	54.2%	*Journal of the American Chemical Society.* ***2017****, 139, 1921*
L-NCNTs	808	58.8%	*International Journal of Biological Macromolecules.* ***2023,*** *238, 124127*
PPy NPs	808	45%	*Chemical Communications.* ***2012****, 48,* 8934

Table S2 Performance comparison of the current work with the reported advanced bifunctional electrocatalysts.

Catalysts	**OER**	**ORR**	**Δ*E*(V**	**Ref.**

	E_{10} (V)	Electrolytes	$E_{1/2}$ (V)	J_L (mA cm^{-2})	Electrolytes	)	
$NiCo_2S_4$@NiFe LDH/N-rGO-Light	1.456	1 M KOH	0.82	-4.08	0.1 M KOH	0.636	**This work**
$NiCo_2S_4$@NiFe LDH/N-rGO	1.492		0.809	-4.22		0.683	
P-NCO/ NCN-CF@CC	1.578	0.1 M KOH	0.828	-	0.1 M KOH	0.75	*Advanced Functional Materials **2023**, 33, 2302883*
Ni@CNx	1.59	1 M KOH	0.74	-	0.1 M KOH	0.85	*Advanced Functional Materials **2023**, 2300405*
$CuCo_2O_{4-x}S_x$/NC-2	1.57	0.1 M KOH	0.75	-	0.1 M KOH	0.82	*Advanced Materials **2023**, 2303488*
Fe-N-C/Fe_3C-op	1.579	0.1 M KOH	0.911	-	0.1 M KOH	0.668	*Advanced Science, 2301656*
FeCoNiMoW	1.463	1 M KOH	0.71	-	0.1 M KOH	0.753	*Advanced Materials, 2023, 35, 2303719*
$NiCo_2S_4$/HCS-3	1.54	0.1 M KOH	0.89	-	0.1 M KOH	0.65	*Advanced Functional Materials **2023**, 2300579*
$Co^{II}TP[Co^{III}C]_2$	1.642	0.1 M KOH	0.72	-	0.1 M KOH	0.922	*Angewandte Chemie*

							International Edition ***2023****,62, e2023022*
COP_{BTC}-Co	1.627	1 M KOH	0.864	-	1 M KOH	0.76	*Advanced Functional Materials****2023****, 2303235*
Fe-Se/NC	1.623	1 M KOH	0.925	-5.5	0.1 M KOH	0.698	*Angewandte Chemie International Edition* ***2023****, 62, e20221919*
S-LDH/NG	1.47	0.1 M KOH	0.69	-4.78	0.1 M KOH	0.78	*Adv. Funct. Mater.* ***2023****, 33, 2212233*
G@Co_3O_4	1.62	0.1 M KOH	0.78	-5.1	0.1 M KOH	0.84	*Renewables*, **2023**, *1*, 73
CrMnFeCoNi	1.495	1 M KOH	0.761	-	0.1 M KOH	0.734	*Energy Storage Materials,* ***2023*** *58, 287–298*
Co-CNHSC-3	1.58	1 M KOH	0.84	-	0.1 M KOH	0.74	*Carbon Energy.* ***2023****, 5, e317*
CoP_3/CeO_2/C-2	1.569	1 M KOH	0.752	-	0.1 M KOH	0.817	*Applied Catalysis B: Environmental* ***2023,*** *321, 122029*
Co@C-CoNC	1.638	0.1 M KOH	0.906	-6.18	0.1 M KOH	0.732	*Nano-Micro Lett.* ***2023****, 15, 48*
NiFe-LDH/Fe_1-N-C	1.55	1 M KOH	0.9	-5.83	0.1 M	0.65	*Advanced Energy*

					KOH		*Materials*, ***2023***, *2203609*
$Fe_2N/CoFe_2O_4$-PCS	1.53	1 M KOH	0.868	-5.32	0.1 M KOH	0.662	*Chemical Engineering Journal,* ***2023****,471, 144639*
POP-Fe/Ni-900	1.62	1 M KOH	0.82	-5.26	0.1 M KOH	0.8	*Journal of Materials Chemistry A,* ***2023****, 11, 12194–12201*
m-Fe/N-C@CNT	1.568	1 M KOH	0.832	-5.3	0.1 M KOH	0.736	*Applied Catalysis B: Environmental* ***2023,*** *327,122443*
CoSA&CoNP-1	1.62	0.1 M KOH	0.86	-5.53	0.1 M KOH	0.76	*Small Methods,* ***2023****, 7, 2201371*
Fe3C|Fe–N–C	1.638	0.1 M KOH	0.848	-5.165	0.1 M KOH	0.79	*Chemical Engineering Journal,* ***2023****, 454, 140512*
CoNi-CoN_4-HPC-900	1.7	0.1 M KOH	0.78	-6.85	0.1 M KOH	0.92	*Nano Energy* ***2022****, 99,107325*
Fe_1Co_3−NC-1100	1.579	0.1 M KOH	0.877	-	0.1 M KOH	0.702	*ACS Catalysis* ***2022****, 12, 1216−1227*
Co-N-C	1.65	0.1 M KOH	0.86	-5.7	0.1 M KOH	0.79	*Science Advances,* ***2022****, 8, eabn5091*
Co-CoN_4@NCNs	1.54	1 M KOH	0.83	-6.0	0.1 M	0.71	*Advanced*

					KOH		*Functional Materials, **2022**, 32, 2207331*
Co SA-NDGs	1.58	0.1 M KOH	0.87	-5.8	0.1 M KOH	0.71	*Nature Communications, **2022**, 13, 3689*
Co/CoO@NSC	1.61	0.1 M KOH	0.835	-	0.1 M KOH	0.775	*Journal of Energy Chemistry, **2022**, 64, 385*
Co_3O_4/Mn_3O_4/N-rGO	1.59	0.1 M KOH	0.86	-6.0	0.1 M KOH	0.73	*Journal of Energy Chemistry, **2022**, 68, 679*
O–Co–N/C	1.52	1 M KOH	0.85	-5.2	0.1 M KOH	0.67	*Advanced Functional Materials, **2022**, 32, 2200763*
$NiMnCoO_4$-AC	1.57	1 M KOH	0.82	-5.0	0.1 M KOH	0.75	*Pnas, **2022**, 119, e2202202119*
FePc||CNT||NiCo/CP	1.588	0.1 M KOH	0.902	-4.6	0.1 M KOH	0.686	*Advanced Energy Materials*, **2022**, *12*, 2202984
Fe-N-C/N-OMC	1.761	0.1 M KOH	0.93	-4.07	0.1 M KOH	0.83	*Applied Catalysis B: Environmental*, **2021**, *280*, 119411
$NiFe_2O_4$	1.559	1.0 M KOH	-	-	-	-	*Proceedings of the National Academy of*

							Sciences of the United State of America, **2021**, *118*, e2023421118
Co_9S_8/MnS-USNC	1.59	1 M KOH	0.90	3.92	0.1 M KOH	0.694	*Journal of Materials Chemistry A*, **2021**, *9*, 22635
N-HCTs@$NiCo_2O_4$	1.56	0.1 M KOH	0.81	6.02	0.1 M KOH	0.75	*Journal of Electroanalytical Chemistry*, **2021**, *902*, 115804
Co_4N@NC	1.52	0.1 M KOH	0.84	-	0.1 M KOH	0.679	*Applied Catalysis B: Environmental*, **2020**, *275*, 119104
N-Co-Mo-GF/C	1.56	0.1 M KOH	0.83	-	0.1 M KOH	0.73	*ACS Catalysis*, **2020**, *10*, 4647
CoPc-GO	1.6	1 M KOH	0.76	-	0.1 M KOH	0.84	*ACS Nano*, **2020**, *14*, 13279
FeCo(a)-ACM	1.6	1 M KOH	0.9	-	0.1 M KOH	0.7	*Energy Storage Materials*, **2020**, *24*, 402
LDH-POF	1.48	0.1M KOH	0.8	-	0.1M KOH	0.68	*Advanced Functional Materials*, **2020**, *30*, 2003619

Table S3 Comparison of the liquid ZABs performance of this work with recent reports.

Catalysts	△E (V)	Power density (mW cm^{-2})	Current density (mA cm^{-2})	Cycling number	Ref.
$NiCo_2S_4$@NiFe LDH/N-rGO-Light	0.636	206	25	8285	***This work***
			10	7437	
$NiCo_2S_4$@NiFe LDH/N-rGO	0.683	188	25	3410	
			10	4010	
P/Fe−N−C	0.634	269	10	576	*Journal of the American Chemical Society 2023**, 145, 6, 3647 − 3655***
Fe-N-C/Fe3C-op	0.668	137.4	5	1150	*Advanced science , 2301656*
FeCoNiMoW	0.753	116.9	8	2000	*Advanced Materials, 2023, 35, 2303719*
Co_2P/CoN_4@NSC-500	-	134.49	5	3484	*Angewandte Chemie International Edition 2023, 62, e202216950*
NiFe-LDH/Fe_1-N-C	0.65	205	2	1200	*Advanced Energy Materials **2023**, 2203609*
$CuCo_2O_{4-x}S_x$/NC-2	0.82	92	10	900	*Advanced Materials, **2023**, 2303488*
$NiCo_2S_4$/HCS-3	0.65	215	10	100	*Advanced Functional Materials, **2023**, 2300579*
COP_{BTC}-Co	0.76	157.7	10	100	*Advanced Functional*

					Materials,***2023***, *2303235*
S-LDH/NG	0.78	165	5	360	*Advanced Functional Materials*, ***2023***, *33, 2212233*
P-Ag-Co(OH)$_2$	0.503	435	5	500	*Advanced Functional Materials*, ***2023***, *2301947*
Co SAs/AC@NG	-	221	10	400	*Advanced Functional Materials*, **2023**, *33, 2209726*
POP-Fe/Ni-900	0.8	256	5	450	*Journal of Materials Chemistry A,* ***2023***, *11, 12194–12201*
Fe-HPNC/Co$_3$O$_4$	0.571	236	5	495	*Journal of Materials Chemistry A,* ***2023***, *11, 1312–1323*
RuFe−N−C	0.63	139.9	5	600	*ACS Materials Lett.* ***2023***, *5, 1656−1664*
CrMnFeCoNi	0.734	116.5	8	720	*Energy Storage Materials,* ***2023***,*58, 287–298*
Co-CNHSC-3	0.74	118.1	10	200	*Carbon Energy.* ***2023***;*5:e317*
VM-NC	0.631	165	10	1200	*Applied Catalysis B: Environmental,* ***2023***,*335, 122895*
β-FeCo-PCNF	0.595	196.5	10	5010	*Applied Catalysis B: Environmental*

					***2024**,340, 123231*
Co@C-CoNC	0.732	162.8	2	300	*Nano-Micro Lett, **2023**,15:48*
$Fe_2N/CoFe_2O_4$-PCS	0.662	225	10	943	*Chemical Engineering Journal, **2023**,471, 144639*
CoP_3/CeO_2/C-2	0.817	150	5	360	*Applied Catalysis B: Environmental, **2023**, 321, 122029*
Pt_{SA}–PtCo NC/N–CNT-900	0.622	110.6	10	660	*Small **2023**, 2304294*
CoP/CoO@ MNC-CNT	0.622	152.8	10	1500	*Small **2023**, 2206341*
FeCoNiSx	-	257.2	10	2000	*Advanced Materials*, **2022**, 2204247
			30	-	
Co-N-C	0.79	161.8	5	480	*Science Advances, **2022**, 8, eabn5091*
			25	200	
Fe_1Co_3−NC-1100	0.702	372	10	600	*ACS Catalysis **2022**, 12, 1216−1227*
Ni/Fe-NC/NCF/CC	0.588	162	10	2150	*Energy Environ. Mater.**2022**,0, e12541*
Co-CoN_4@NCNs	0.71	118.8	10	1500	*Advanced Functional Materials, **2022**, 32, 2207331*
FePc||CNTs||NiCo/CP	0.686	219.5	10	700	*Advanced Energy Materials*, **2022**, *12*, 2202984

Co SA-NDGs	0.71	251.4	5	350	*Nature Communications*, **2022**, *13*, 3689
			10	800	
NiMnCo-AC	0.75	187.7	10	600	*Pnas, **2022**, 119, e2202202119*
Co_3O_4/Mn_3O_4/N-rGO	0.73	194.6	1	1200	*Journal of Energy Chemistry, **2022**, 68, 679*
			5	1200	
			10	300	
Co/CoO@NSC	0.775	187.6	10	450	*Journal of Energy Chemistry, **2022**, 64, 385*
O–Co–N/C	0.67	143	2	450	*Advanced Functional Materials **2022**, 32, 2200763*
FeCo/Se-CNT	0.76	173.4	5	210	*Nano Letters*, **2021**, *21*, 2255
CoNC@LDH	0.63	173	10	3630	*Advanced Materials, **2021**, 33, e2008606*
			25	1750	
			100	29	
CNT@SAC-Co/NCP	0.74	172	20	1260	*Advanced Functional Materials*, **2021**, *31*, 2103360
$NiCo_2S_4$/ZnS	0.65	160	5	260	*Angewandte Chemie International Edition*, **2021**, *60*, 19435
Co_2P/CoNPC	0.797	116	10	-	*Advanced Materials*, **2020**, *32*, e2003649
FePc-GO	0.76	-	-	-	*ACS Nano*, **2020**, *14*,

					13279
CoP@PNC-DoS	0.781	138.57	30	350	*Energy Storage Materials*, **2020**, *28*, 27
Ni|MnO/ CNF	0.763	138.6	10	350	*Advanced Functional Materials*, **2020**, *30*, 1910568
FeCo–N–C	0.704	150	5	360	*Journal of Materials Chemistry A*, **2020**, *8*, 9355
PdMo	-	154.2	10	350	*Nature **2019** 574, 81-85*

Table S4 Comparison of the FZAB performance of this work with recent reports.

Catalysts	**Electrolyte**	**Working temperature (°C)**	**Ionic conductivity (mS/cm)**	**OCV (V)**	**Power density (mW/cm^2)**	**Specific capacity (mAh/g)**	**Energy density (Wh/kg)**	**Cycling number @ Current density (mA/cm^2)**	**Ref.**
$NiCo_2S_4$@NiFe LDH/N-rGO	Alkalified PAA	60	298.4	-	176.3 Light	778.63 Light	-	430@1 Light	***This work***
					162.9	755.95		100@1	
		25	273.79	1.489 Light	151.7 Light	780.95 Light	-	1300@1 Light	
				1.44	111	761.04		1312@1	
		-40	72.07	1.363 Ligh	49.95 Light	738.23 Light	-	3480@1 Light	

				1.327	46.47			1300@1	
CoCNTs/PNAs	PAA	25	-	1.37	-	-	-	200@5 250@3 260@2	*Advanced Energy Materials*, **2023**, *13, 2202871*
NF/CCO/FCH	PAA	25	-	1.448	35.2	-	-	81@0.5	Applied Catalysis B: Environmental, 2023, 325, 122332
Fe-Se/NC	PAM	25	30	1.47	135	764	939	1090@20	Angewandte Chemie International Edition ***2023***, *62, e202219191*
		-40	18	1.44	-	697	753	4041@1 725@5	
Co/CoO@NSC	PANa-KOH	25	-	1.43	82.7	680	911.2	858@2	*Journal of Energy Chemistry,* ***2022****, 64, 385*
CoP_3/CeO_2/C-2		25		1.401		-	-	1001	*Applied Catalysis B: Environmental* ***2023,*** *321, 122029*
CoP/CoO@ MNC-CNT	PVA-KOH	25	-	1.409	-	-	-	1200@5	*Small* ***2023****, 2206341*

FeCoNiMoW	(PVA)-KOH-gel	25	-	1.34	40.12	-	-	90@5	*Advanced Materials 2023, 35, 2303719*
Fe3C|Fe–N–C	PANa	25	-	1.414	63	-	-	1000@2	*Chemical Engineering Journal 454* ***2023****, 140512*
S–LDH/NG	self-made gel polymer electrolyte	25	-	1.43	86	-	-	50@2	*Advanced Functional Materials* ***2023****, 33, 2212233*
Pt/C RuO_2	MC/PAM-PDMC	25	215	1.468	132	758@2	-	1020@2	*Advanced Materials*, **2022**, *34*, 2110585
CoNi-CoN_4-HPC-900	PVA	25	-	1.5	27	-	-	162@5	*Nano Energy 99,* ***2022****, 107325*
H-NiFe/CNF	PVA	25	-	-	85.3	-	-	120@1	*Nano Energy*, **2022**, *104,* 107941
Co SA-NDG	PAM	-40	0.4	-	21.9	778.4	918.5	436@2	*Nature Communications*, **2022**,
		-60	0.087	-	-	-	-	272@1	

									13, 3689
FeMn-DSAC	PAM-MMT KOH+Zn(OAc)$_2$	-40	27.1	1.44	30	631	725	81@ 2	*Angewandte Chemie International Edition*, **2022**, *61*, e202115219
NiMnCoO$_4$-AC	PVA-KOH	25	-	1.377	-	-	-	-	*Proceedings of the National Academy of Sciences of the United State of America*, **2022**, *119*, e2202202119
Co/MnO@N,S-CNT/NFs	PAA+KOH	25	-	1.34	62.5	-	-	45@1	*Applied Catalysis B: Environmental*, **2021**, *295*, 120281
FeCo–P/N–C–F	PVA	-30	90	1.47	63.3	699	798	500@5	*Energy & Environmental Science*, **2021**, *14*, 4926
		25	265		128.8	740	891	500@5	
CoMn$_{1.5}$Ni$_{0.5}$O$_4$	PAMC	-20	-	1.44	35.8	-	-	22@5	*Chemical*

		25	96.3	-	85.8	-	-	190@5	*Engineering Journal*, **2021**, *417*, 129179
		2	-	-	-	-	-	200@5	
Pt/RuO_2	PANa-St-0.5/KOH	25	82	1.40	60.7	673	-	86@1	*Composites Part B: Engineering*, **2021**, *224*, 109228
		-20	56.7	1.38	21.9	714	-	133@1	
P,S-Co_xO_y/Cu@CuS NWs	PVA-KOH	25	-	1.383	130	-	-	25h@5	*Advanced Functional Materials*, **2020**, *31*, 2007822
Pt/C-RuO_2	PAM/PAA	25	-	1.42	11.8	663.25	769.37	100@1	*ACS Sustainable Chemistry & Engineering*, **2020**, *8*, 11501
		0			9.45	612.45	689.01		
		-20		1.44	7.9	506.17	556.79	100@1	
Co_3O_4	PAMPS-K	25	105	1.35	73.9	764.7	850.2	72@1	*ACS Applied Materials & Interfaces*, **2020**, *12*, 11778
		0	-	-	65	758.5	831.9	72@1	
		-20	-	1.38	52.4	754.2	824.6	72@1	
MnO_2/NRGO-Urea	PAM	25	215.6	1.32	105	720	-	140@5	*Journal of Power*

									Sources, **2020**, *450*, 227653
NiO/CoO TINW	PAA+KOH	-10	-	-	-	328.57	364.45	42@1	*Angewandte Chemie International Edition*, **2019**, *58*, 9459
		-5		-		373.17	413.44	36@1	
		0		-		570.80	658.70	54@1	
		10		-		772.05	897.28	54@1	
		25		1.354		842.58	996.44	99@1	
CoOx/N-RGO	PVA-KOH	25	-	1.39	120	-	-	60@6	*Advanced Materials*, **2019**, *31*, 1807468
Fe-N-C@CNT	PANa	25	280	1.48	108.6	800	930	660@5	*Advanced Energy Materials*, **2019**, *9*, 1803046
FeCoNiCuMo HEA	PVA	25	-	-	72	-	-	210@5	*Chemical Engineering Journal, **2024**, 488, 151093*
Fe_5Co_5@NPC	PAM-DMSO	70	-	-	160	-	-	24@2	*Advanced Energy Materials **2024**, 14, 2303011*
		25			140			1180@2	
		-40			110			2600@2	
CoFe-NiFe/NC	PAA	25	-	1.47	124.5	809	990	-	*Advanced Functional*

									*Materials .**2024**, 34, 2402933*
NHCF-900	PVA	25	-	1.5	155.6	801.2	952.4	330@2	*Small **2024**, 2311675*
FeCo-NC	PAA	60	-	1.44	156	1002.57	1393.32	330@2	*Advanced Functional Materials .**2023**, 33, 2212299*
		30		1.51	133	747	971.3	1200@2	
		0		1.45	80	950	-	2000@2	
		-30		1.48	34	602.48	747.07	2000@2	
Pt/C-RuO_2	PAMNa-CMCS	60	-	-	146.38	-	-	-	*Chemical Engineering Journal 468 **2023** 143836*
		20	145.63		120.87	775.82			
		-20	-		90.4	-			

Table S5. Cycling performance summary of ZABs based on $NiCo_2S_4$@NiFe LDH/N-rGO.

	Battery type (liquid / flexible)	Cycling number	Cycling time (h)	Current density (mA cm^{-2})	Light exposure	Temperature (℃)
1	liquid	4010	1336.67	10	No	25
2		7437	2479	10	Yes	25
3		3410	1136.67	25	No	25
4		8285	2761.67	25	Yes	25
5		255	85	50	No	25
6		340	113.33	50	Yes	25
7	flexible	1300	130	1	No	-40
8		3480	348	1	Yes	-40
9		538	53.8	5	No	25
10		325	32.5	5	Yes	25
11		1312	131.2	1	No	25
12		1300	130	1	Yes	25
13		100	10	1	No	60
14		430	43	1	Yes	60

Table S6. Peak area ratio of Ni^{3+}/Ni^{2+} of as-prepared $NiCo_2S_4$@NiFe LDH/N-rGO.

Sample	Ni^{3+}/Ni^{2+} within *Ni* $2p_{3/2}$	Ni^{3+}/Ni^{2+} within *Ni* $2p_{1/2}$
Pristine sample	0.41	0.37

Table S7. Peak area ratio of Ni^{3+}/Ni^{2+} of $NiCo_2S_4$@NiFe LDH/N-rGO after photothermal-assisted OER and subsequent photothermal-assisted ORR tests.

Samples	Ni^{3+}/Ni^{2+} within *Ni* $2p_{3/2}$	Ni^{3+}/Ni^{2+} within *Ni* $2p_{1/2}$
OER with light	2.65	3.87
Subsequent ORR with light	0.34	0.35

Table S8. Peak area ratio of Ni^{3+}/Ni^{2+} of $NiCo_2S_4$@NiFe LDH/N-rGO after OER (without light) and subsequent ORR tests (without light) as control experiments.

Samples	Ni^{3+}/Ni^{2+} within *Ni* $2p_{3/2}$	Ni^{3+}/Ni^{2+} within *Ni* $2p_{1/2}$
OER without light	2.38	3.73
Subsequent ORR without light	0.81	0.49

References

1. F. Ye, A. Ayub, R. Karimi, S. Wettig, J. Sanderson and K. P. Musselman, *Adv. Mater.*, 2023, **35**, e2301129.
2. Z. Zhao, C. Chen, W. Wu, F. Wang, L. Du, X. Zhang, Y. Xiong, X. He, Y. Cai, R. T. K. Kwok, J. W. Y. Lam, X. Gao, P. Sun, D. L. Phillips, D. Ding and B. Z. Tang, *Nat. Commun.*, 2019, **10**, 768.
3. G. Kresse and J. Hafner, *Phys. Rev. B*, 1993, **47**, 558.
4. G. Kresse and J. Hafner, *Phys. Rev. B*, 1994, **49**, 14251-14269.
5. J. P. Perdew, K. Burke and M. Ernzerhof, *Phys. Rev. Lett.*, 1996, **77**, 3865-3868.
6. G. Kresse and D. Joubert, *Phys. Rev. B*, 1999, **59**, 1758-1775.
7. P. E. Blochl, *Phys. Rev. B*, 1994, **50**, 17953-17979.
8. J. K. Nørskov, J. Rossmeisl, A. Logadottir, L. Lindqvist, J. R. Kitchin, T. Bligaard and H. Jónsson, *J. Phys. Chem. B*, 2004, **108**, 17886-17892.
9. L. I. Bendavid and E. A. Carter, *J. Phys. Chem. C*, 2013, **117**, 26048-26059.
10. Y. Liu, Y. Huang and X. Duan, *Nature*, 2019, **567**, 323.
11. D. Liu, Z. Liu, J. Zhu and M. Zhang, *Mater. Horiz.*, 2023, **10**, 5621.